ORIGINAL ARTICLE

**Junxiang Yang · Hyundong Kim · Chaeyoung Lee ·
Sangkwon Kim · Jian Wang · Sungha Yoon · Jintae Park ·
Junseok Kim**

Phase-field modeling and computer simulation of the coffee-ring effect

Abstract In this study, we propose a novel computational model for simulating the coffee-ring phenomenon. The proposed method is based on a phase-field model and Monte Carlo simulation. We use the Allen–Cahn equation with a pinning boundary condition to model a drying droplet. The coffee particles inside the droplet move according to a random walk function with a truncated standard normal distribution under gravitational force. We perform both two-dimensional and three-dimensional computational experiments to demonstrate the accurate simulation of the coffee-ring phenomenon by the proposed model.

J. Yang · H. Kim · C. Lee · S. Kim · J. Wang · S. Yoon · J. Park · J. Kim (✉)
Department of Mathematics, Korea University, Seoul 02841, Republic of Korea
E-mail: cfdkim@korea.ac.kr

J. Yang
E-mail: nexusxiang@outlook.com

H. Kim
E-mail: rlagusehd@korea.ac.kr

C. Lee
E-mail: chae1228@korea.ac.kr

S. Kim
E-mail: ksk8863@korea.ac.kr

J. Wang
E-mail: super_wj150@korea.ac.kr

S. Yoon
E-mail: there122@korea.ac.kr

J. Park
E-mail: jintae2002@korea.ac.kr

1 Introduction

Droplet evaporation on a substrate is an important phenomenon in the field of soft matter physics. This phenomenon represents problems related to fluid dynamics, the physics of solid particles, properties of solid substrates, and heat transfer [1]. Based on the complexity of droplet evaporation, many researchers have employed evaporation dynamics in various real-world applications, such as self-assembly techniques [2], medical tests [3,4], coating and printing engineering [5], and DNA mapping [6]. In comparison with pure liquid droplets, nanoparticle-suspended liquid droplets (NSLDs) are more common in scientific and engineering fields. NSLDs have a variety of applications in numerous industrial fields, including biomedicine [7,8], optics [9,10], inkjet printing [11,12], painting [13,14], ceramics [15], and wastewater treatment [16]. Ring-like deposition patterns containing nanoparticles, which are referred to as "coffee-ring stains," can be observed when an NSLD evaporates on a substrate [17]. Conway et al. [18] experimentally determined that contact angles cause ring-like pattern formations during the evaporation of colloidal suspensions. In general, there are two main types of contact line conditions during the evaporation of NSLDs on a substrate. One is a pinning condition with a fixed contact area, and the other is a nonpinning condition with a fixed contact angle. Evaporation with a pinning condition forces the random particles inside a droplet to move toward the pinned contact line. The particles are then deposited around the contact line. This physical process produces a coffee-ring stain. Weon and Je [19] discussed the differences between pure and colloidal droplets in terms of spreading and drying phenomena and proposed a self-pinning mechanism based on confined colloidal particles at contact lines. A variety of pattern formations, such as ring-like depositions or more complex patterns, can be generated by the evaporation of colloidal drops. Heat transfer occurs through convection at the evaporating free surface, and mass transfer occurs through the diffusion of liquid vapor into the atmosphere. The convection–diffusion behavior of nanoparticles in suspended liquids determines the resulting deposition patterns [20]. The evaporation of liquid and the convective transfer of nanoparticles to the contact line are considered to be the most important mechanisms for ring-like deposition. Segregation toward the edge of an NSLD is a general phenomenon; however, controlling the distribution of solutes during drying is a critical issue because the effects of deposition may be considered as desirable [21,22] or undesirable [23–25] properties in a bunch of scientific research. In an extension to their previous study, the authors of [17] determined that colloidal particles are deposited along the contact lines in droplets and that various patterns are generated by self-pinning [26,27]. Hu and Larson [28] determined that the suppression of the Marangoni flow, which is a recirculating flow induced by surface tension gradients generated by the latent heat of deposition, plays an important role in generating depositions of colloidal particles at the edges of evaporating droplets, as well as at pinned contact lines, leading to the coffee-ring effect [17].

Regarding numerical approaches, a series of studies on the pattern formation of evaporating suspensions of dissolved nanoparticles have been conducted based on Monte Carlo models [29–31] and Brownian dynamics [32,33]. The authors of [29] constructed a model to demonstrate the drying phenomena of a liquid droplet containing nanoparticles, and the author of [30] studied the nonequilibrium dewetting processes of nanoparticle-containing solutions and discussed various patterns, including ring-like patterns and other structures, based on modeling. A phenomenon called "flower-like" pattern formation was simulated using a two-dimensional (2D) kinetic Monte Carlo model in [31]. The formation of coffee stains [34] requires boundary conditions, such as pinning boundaries, as depicted in Fig. 1.

In this study, we propose a novel computational model for the simulation of the coffee-ring phenomena using a phase-field model and Monte Carlo simulation. Phase-field models have been extensively applied
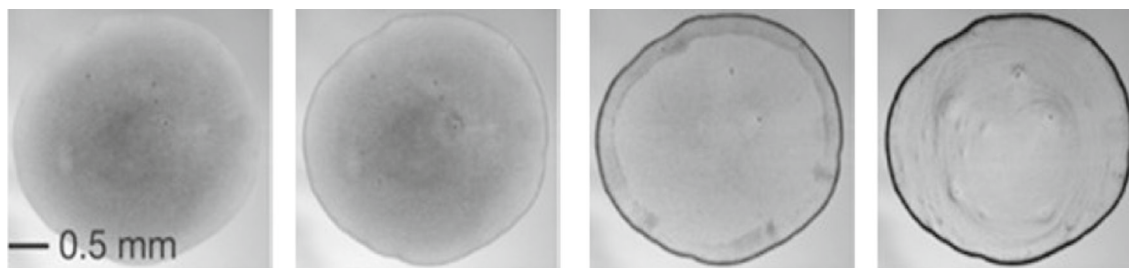

Fig. 1 Evolution of a droplet of particle suspension evaporating, from left to right. Adapted from Yunker et al. [34] with permission from Nature Publishing Group
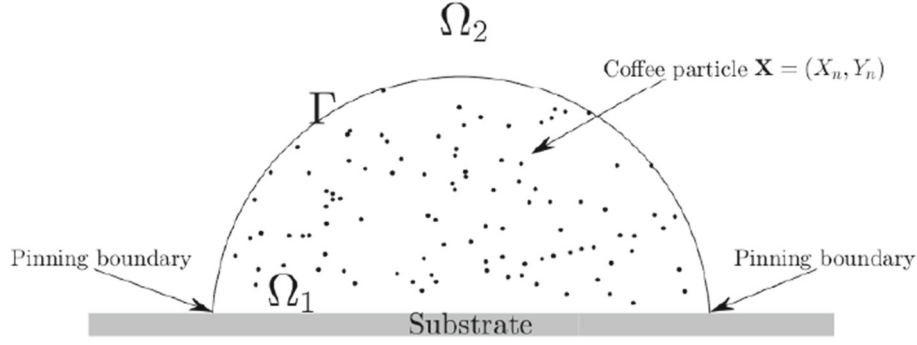
Fig. 2 Schematic illustration of a droplet containing particles

in simulations of material and fluid dynamics [35–40]. For modeling a drying droplet, the Allen–Cahn (AC) equation with a pinning boundary condition [41] is adopted. The coffee particles inside a droplet move according to random walk with a truncated standard normal distribution under gravitational force.

The remainder of this paper is organized as follows. In Sect. 2, we present the governing equations for the phase-field methods. In Sect. 3, we propose numerical solutions. Numerical results are presented in Sect. 4. Finally, conclusions are drawn in Sect. 5.

2 Governing equations

In this paper, we consider two fluids in a 2D domain $\Omega = \overline{\Omega}_1 \cup \overline{\Omega}_2$, where Ω_1 and Ω_2 are liquid and air phases, respectively. The interface between two phases is defined as $\Gamma = \overline{\Omega}_1 \cap \overline{\Omega}_2$, as depicted in Fig. 2. Here, the phase field in the fluid Ω_1 is defined by $\phi \approx 1$, and the phase field in the fluid Ω_2 is defined by $\phi \approx -1$ and $\phi = 0$ at the interface Γ. The sharp interface between the fluids is thin; however, the interfacial forces are smoothly distributed in transition regions with nonzero thickness [42]. The coffee particles are defined as Lagrangian points in Ω_1.

For simplicity, we consider Brownian particles with only mass and no volume. Additionally, the interface moves based on the mean curvature with a pinning boundary condition, which effectively simulates evaporation. We consider the following equations governing the motion of the interface between two fluids and Brownian particles:

$$\frac{\partial \phi(\mathbf{x}, t)}{\partial t} = -\frac{F'(\phi(\mathbf{x}, t))}{\epsilon^2} + \Delta \phi(\mathbf{x}, t), \tag{1}$$

$$\frac{d\mathbf{X}}{dt} = \frac{\alpha}{\sqrt{dt}} \boldsymbol{\psi}(\mathbf{X}) + \mathbf{g}(\mathbf{X}), \tag{2}$$

where $F(\phi) = 0.25(\phi^2 - 1)^2$, ϵ is the interface width, and $\mathbf{X}$ is a Lagrangian variable representing the particles. $\mathbf{x} = (x, y)$ for $2D$ and $\mathbf{x} = (x, y, z)$ for $3D$ are Cartesian coordinates, and t is time. The scaled gravitational force is $\mathbf{g} = (0, -g)$ for $2D$ and $\mathbf{g} = (0, 0, -g)$ for $3D$. Equation (1) is the AC equation [43] with a pinning boundary condition, which is used for simulating volume changes in a droplet caused by evaporation. We use either a Dirichlet boundary or homogeneous Neumann boundary condition in these governing equations. Equation (2) is derived from the Langevin Eq. [44] with the assumption of zero force acting on a particle, implying that the mass times the second derivative of the vertical position of a particle is negligible. Here, $\boldsymbol{\psi}(\mathbf{X})$ represents a random force on a Brownian particle. In 2D space, let θ be a random variable with a continuous uniform distribution on the interval $[0, \pi]$. We select a random variable ρ with a truncated standard normal distribution such that the probability density function is $f(\rho) = e^{-0.5\rho^2}/\sqrt{2\pi}$, which is widely employed to characterize physical phenomena. Because the particles cannot be infinitely spread within a droplet, it is reasonable to adopt a truncated normal distribution for the domain of droplet experiments. For additional details, please refer to the reference papers [45–47] and the references therein. We consider a random variable ρ in the range of $[-3, 3]$, which represents 99.7% confidence interval. Then, we define the truncated radial random force as $\boldsymbol{\psi}(\mathbf{X}) = (\rho \cos(\theta), \rho \sin(\theta))$ in the 2D case, see Fig. 3a for a schematic illustration. Similarly, for the 3D case, the truncated spherical random force is defined as
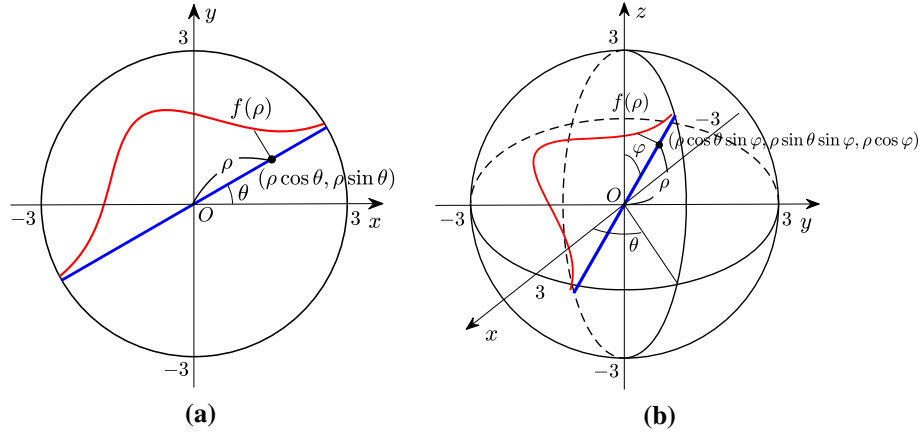
Fig. 3 Schematic illustrations of truncated standard normal distribution for **a** 2D cases and **b** 3D cases
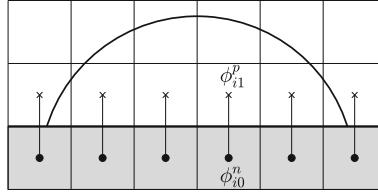

Fig. 4 Pinning boundary condition for the bottom boundary in a 2D space

$\psi(\mathbf{X}) = (\rho \cos(\theta) \sin(\varphi), \ \rho \sin(\theta) \sin(\varphi), \ \rho \cos(\varphi))$, where θ and φ are random variables with continuous uniform distribution on the interval $[0, \ \pi]$, see Fig. 3b for the schematic illustration. In this study, we focused on the simulation of tiny droplets with similar scales to those in [48]. Specifically, the droplet radius was set to $R \le 700\mu$m and the characteristic length $\bar{L}$ is defined as the radius of droplet. Because we considered tiny droplets, the timescale for interfacial evaporation was set to be equal to that of particle movement. The drying rate per surface unit was set to 0.75μm/s, and the characteristic time $\bar{t}$ was set to 1s.

3 Numerical solution

First, we present the numerical solution in 2D space and in the next step we extend the numerical solution into 3D space. The computational domain is defined by $\Omega = (a, b) \times (c, d)$. Let $h = (b - a)/N_x = (d - c)/N_y$ be a spatial step size, where N_x and N_y are positive integers. For $i = 1, \ldots, N_x$ and $j = 1, \ldots, N_y$, let $(x_i, y_j) = (a + (i - 0.5)h, c + (j - 0.5)h)$. For temporal step size Δt, $\phi(x_i, y_j, n\Delta t)$ is simply denoted by ϕ_{ij}^n. To solve Eq. (1), the operator splitting method is applied:

$$\frac{\partial \phi}{\partial t} = \Delta \phi, \tag{3}$$

$$\frac{\partial \phi}{\partial t} = -\frac{F'(\phi)}{\epsilon^2}, \tag{4}$$

We solve Eq. (3) using the explicit Euler's method as follows:

$$\frac{\phi_{ij}^* - \phi_{ij}^n}{\Delta t} = \Delta_h \phi_{ij}^n, \tag{5}$$

where $\Delta_h \phi_{ij}^n = (\phi_{i+1,j}^n + \phi_{i-1,j}^n + \phi_{i,j+1}^n + \phi_{i,j-1}^n - 4\phi_{ij}^n)/h^2$. Next, we solve Eq. (4) analytically using the method of separation of variables as follows:

$$\phi_{ij}^{n+1} = \frac{\phi_{ij}^*}{\sqrt{e^{-\frac{2\Delta t}{\epsilon^2}} + (\phi_{ij}^*)^2 \left(1 - e^{-\frac{2\Delta t}{\epsilon^2}}\right)}}. \tag{6}$$
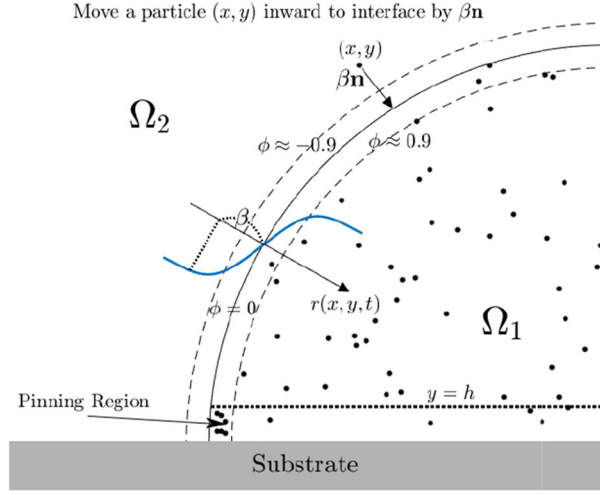
Fig. 5 Schematic illustration of selecting the pinning region and moving particles inward toward the interface. **n** is an inward unit normal vector
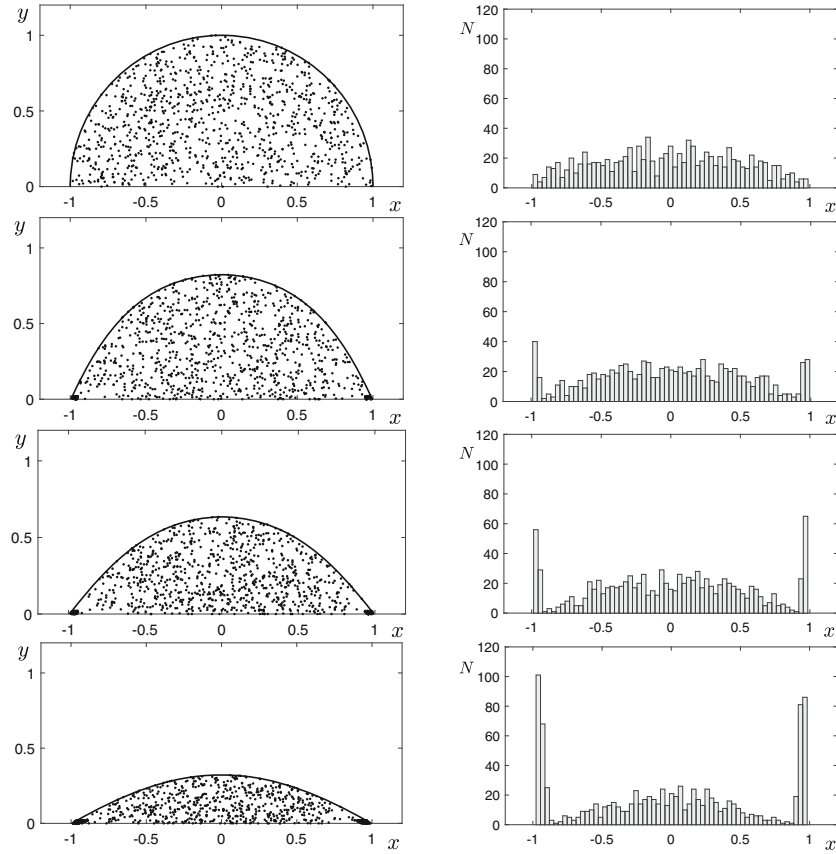

Fig. 6 Evolutions of the droplet and coffee particles (left column), and histogram of the number of coffee particles N (right column). From top to bottom, the times are $t = 0$, $1500\Delta t$, $3000\Delta t$, and $6000\Delta t$

The boundary condition is set to the homogeneous Neumann boundary condition, which is defined as

$$\phi_{0j} = \phi_{1j} \text{ and } \phi_{N_x+1,j} = \phi_{N_x,j} \quad \text{for } 1 \leq j \leq N_y,$$
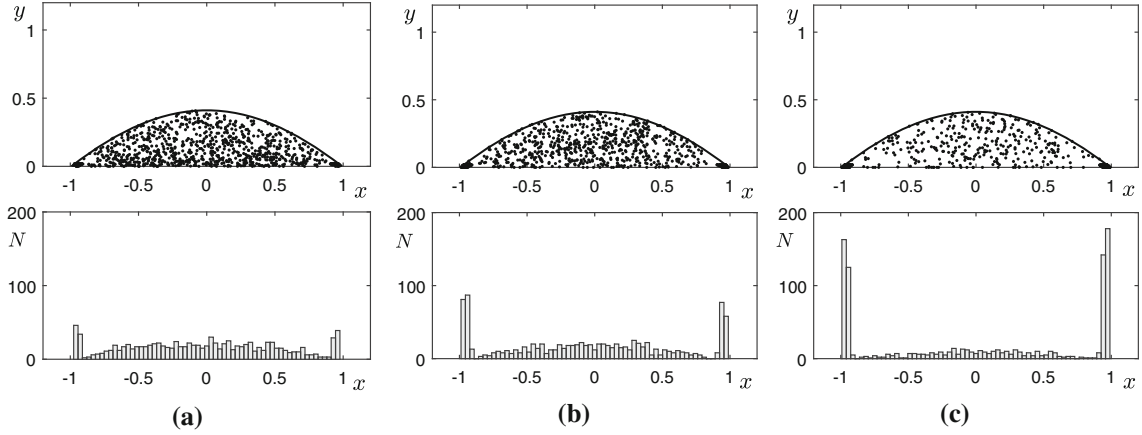$$\phi_{i,N_y+1} = \phi_{i,N_y} \quad \text{for } 1 \leq i \leq N_x.$$

Fig. 7 **a** $\alpha = 40$, **b** $\alpha = 80$, and **c** $\alpha = 160$ at $t = 5000\Delta t$
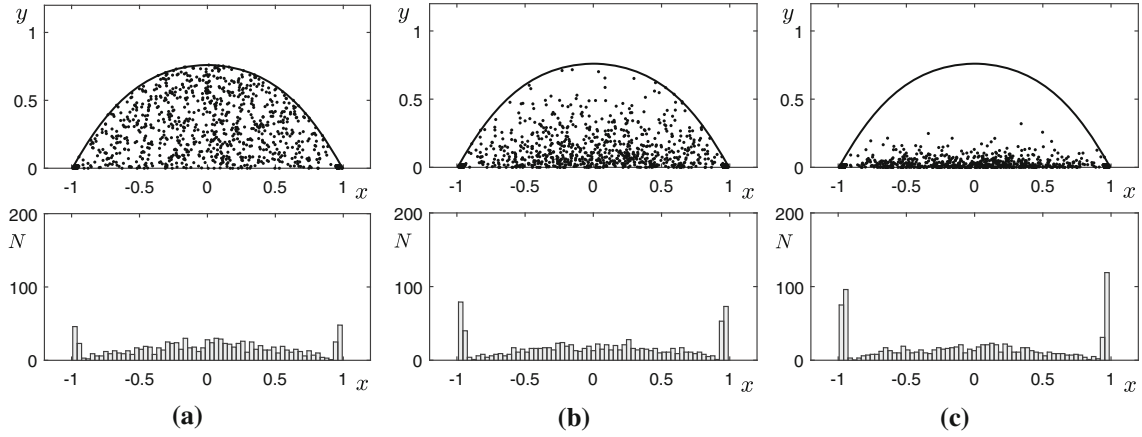

Fig. 8 **a** $g = 1$, **b** $g = 4$, and **c** $g = 16$ at $t = 2000\Delta t$

For the bottom boundary, we use the pinning boundary condition [41], as depicted in Fig. 4, implying

$$\phi_{i0}^n = \phi_{i1}^p \quad \text{for } 1 \le i \le N_x, \; n \ge p,$$

where $\phi_{i0}^p = \phi_{i1}^p$ for the pinning start time $t = p\Delta t$.

For the bottom boundary, we use a pinning boundary condition. A schematic illustration of selecting the pinning region and moving the particles toward the interface along an inward normal vector is illustrated in Fig. 5. $r(x, y, t)$ is a local coordinate system with respect to the interface of the NSLD, implying $\Gamma = \{(x, y) \mid \phi(x, y) = 0\}$. The particles $\{(x, y)\}$ are considered to be fixed to the substrate when $0 \le \phi(x, y) \le 0.9$ and $y \le D/2$, where $D = \sqrt{2}\epsilon \tanh^{-1}(0.9)$. Because the region of $\phi < 0$ is not considered to be a physically possible interfacial region (approximately $0 \le \phi \le 0.9$), we must pull back the particles to the region of $\phi \ge 0$, which is the actual droplet region. To execute this process, we interpolate $\phi(x, y)$ initially because (x, y) is not a point in the numerical grid in general. Then, we derive the inward unit normal vector $\mathbf{n}$ toward the interface. Finally, we evaluate the scale parameter β using local coordinates as follows:

$$\beta = -\sqrt{2}\epsilon \tanh^{-1}\left(\phi(x, y)\right), \tag{7}$$

where $\tanh\left(r/(\sqrt{2}\epsilon)\right)$ is a local profile (see the blue curve of $\phi(r)$ in Fig. 5). Then, the particle (x, y) is moved by a distance $\beta\mathbf{n}$ toward the physically possible interfacial region.
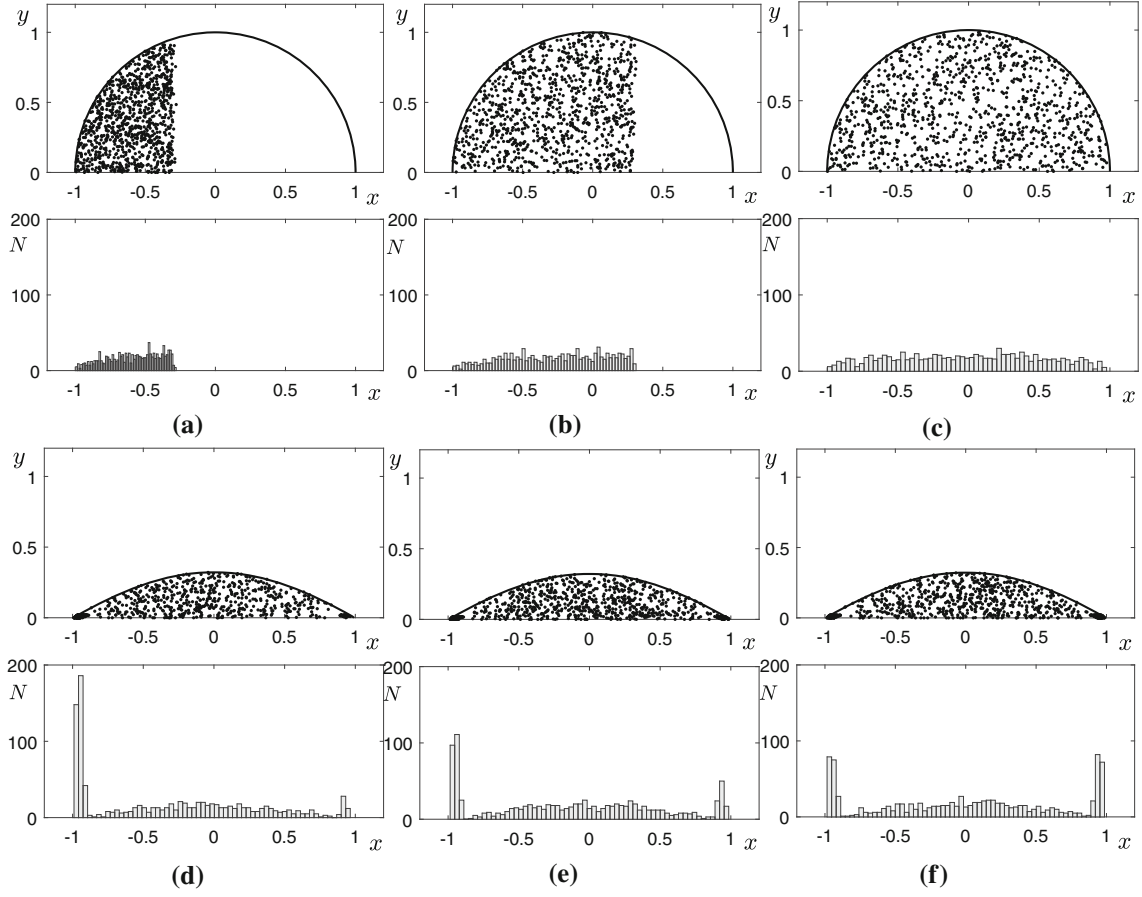
Fig. 9 The first, second, and third columns are $-1 \leq x \leq -0.3$, $-1 \leq x \leq 0.3$, and $-1.0 \leq x \leq 1.0$, respectively. **a**, **b**, and **c** are states at time $t = 0$, **d**, **e**, and **f** are states at $t = 6000\Delta t$
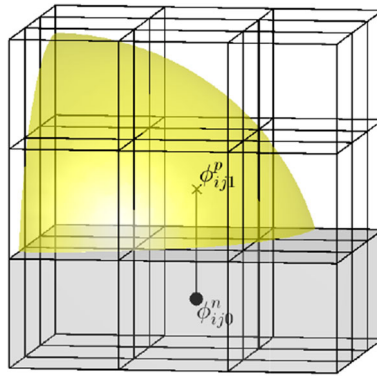

Fig. 10 Pinning boundary condition at the bottom boundary in 3D space

4 Numerical examples

The concentration field over the interfacial region transforms from -0.9 to 0.9 over a distance of approximately $2\sqrt{2}\tanh^{-1}(0.9)$. Therefore, if the value of the concentration field over the interfacial region is computed on m grid points, we can calculate an ϵ value as follows: $\epsilon_m = hm/[2\sqrt{2}\tanh^{-1}(0.9)]$, where h is the space step.
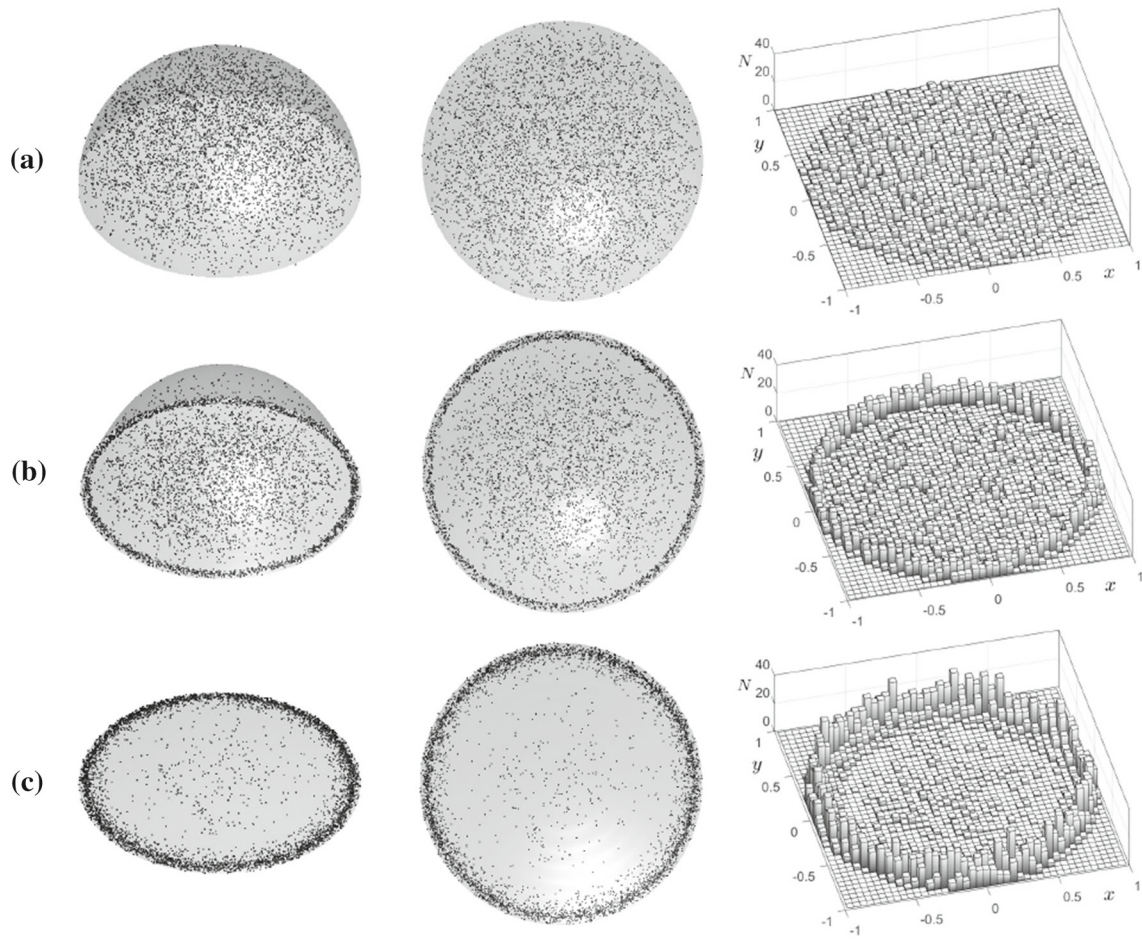
Fig. 11 Temporal evolution of phase-field simulations of the coffee-ring effect with coffee particles in a 3D liquid droplet. Snapshots of phase-field simulations of the coffee-ring effect at **a** $t = 0$, **b** $t = 500\Delta t$, and **c** $t = 3000\Delta t$. Front view and top view of the phase-field simulations of the coffee-ring effect and distribution of coffee particles from left to right

4.1 Coffee particle movement in the 2D space

To confirm the movement of coffee particles in a 2D space, we numerically simulated the evolution of a droplet containing coffee particles. $\Omega = (-1.2, 1.2) \times (0, 1.2)$ is a computational domain, and we consider a semicircle with a center at $(0, 0)$ and radius of 1 as a water droplet. We use the values of $N_x = 120$ and $N_y = 60$ to apply our numerical solution. We adopt the following parameter settings: $h = 0.02$, $\Delta t = 0.25h^2$, $\epsilon = \epsilon_4$, $\alpha = 80$, $p = 0$, and $g = 1$. Additionally, we assume that the number of coffee particles is 1000 and that the particles move randomly. Through this numerical test, we can determine the movement of the coffee particles and confirm the effect of the pinning boundary condition on particle movement. The left column in Fig. 6 presents the time evolution of particle movement. The pinning boundary condition is defined by the points on the x-axis, i.e., $x = -1$ and $x = 1$. The right column in Fig. 6 shows histogram corresponding to the number of coffee particles N in the left column in Fig. 6. This histograms indicates that the coffee particles are highly distributed between -1 and 1. This distribution becomes more apparent over time.

To analyze the effects of the parameters and initial conditions, we simulate a variety of phenomena. First, we consider an initial state satisfying $r < 1$, where $r = \sqrt{x^2 + y^2}$ and $y > 0$. The parameters $\Delta t = 0.25h^2$, $\epsilon = \epsilon_4$, and $g = 1$ are initially set as shown in Fig. 6, and different α values are tested. Figure 7 shows the evolution states of the simulations and histograms of coffee particles. The particles are observed to aggregate faster at the pinning regions with increasing values of α.

Next, we investigate the effects of gravity. Based on the test results described above, we select $\alpha = 80$ and keep the other parameters unchanged. Figure 8 shows the evolution states of the simulations and histograms
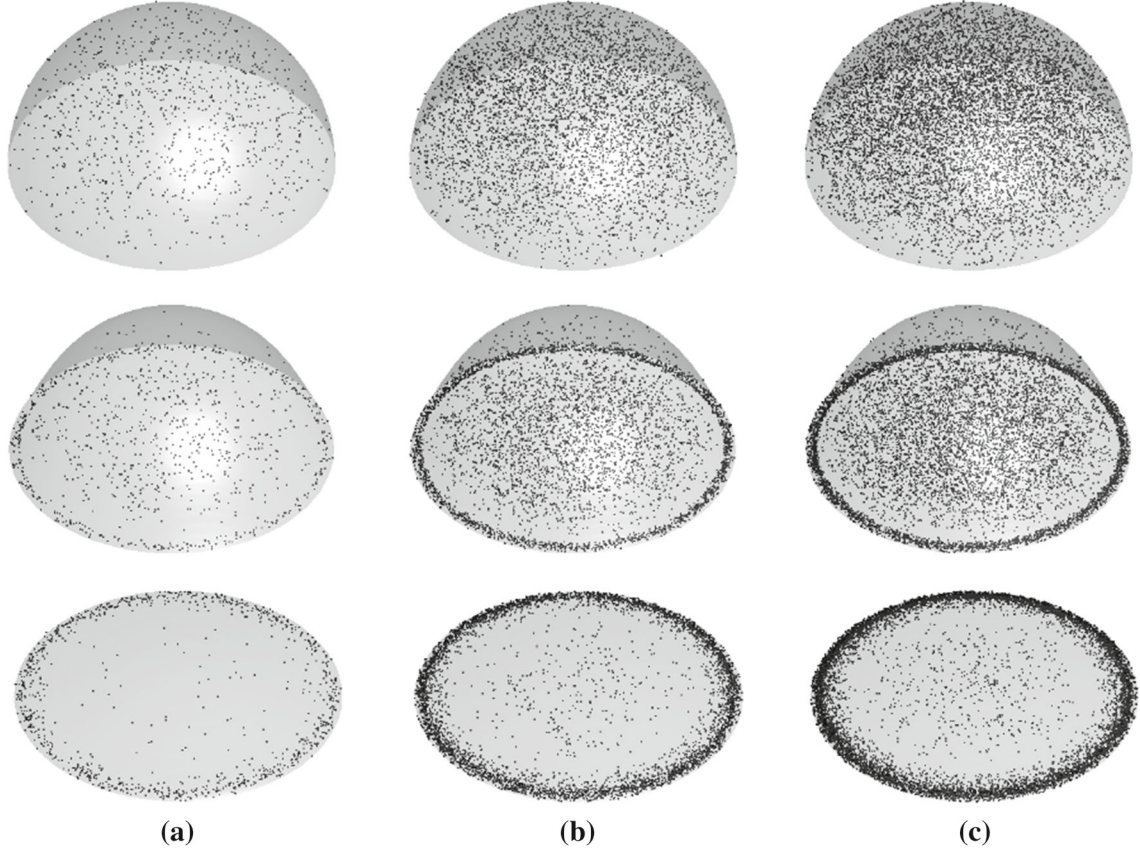
Fig. 12 Temporal evolution of phase-field simulations of the coffee-ring effect with different numbers of coffee particles: **a** 1000, **b** 5000, and **c** 9000. The evolutions from top to bottom in each column are times at $t = 0$, $t = 500\Delta t$, and $t = 3000\Delta t$

of coffee particles with different gravity forces. The results demonstrate that the coffee particles drop more rapidly as the gravity increases.

We investigate the effects of the initial conditions. Values of $g = 1$ and $\alpha = 80$ are taken, and the other parameters are kept unchanged. Figure 9 shows the evolution states of the simulations and histograms of coffee particles with different initial conditions.

4.2 Coffee-ring effect in 3D space

In the following simulations, we consider coffee-ring formation in a 3D space. We extend the numerical solution for a 2D space to a 3D space. In the computational domain $\Omega = (a, b) \times (c, d) \times (e, f)$, we define the cell-centered points $(x_i, y_j, z_k) = (a + (i - 0.5)h, c + (j - 0.5)h, e + (k - 0.5)h)$, where $h = (b - a)/N_x = (d - c)/N_y = (f - e)/N_z$, $i = 1, \ldots, N_x$, $j = 1, \ldots, N_y$, and $k = 1, \ldots, N_z$. Here, N_x, N_y and N_z are positive integers. Let $\phi(x_i, y_j, z_k, n\Delta t)$ be an approximation of ϕ_{ijk}^n. Diffusion term (3) is solved using the explicit Euler's method as follows:

$$\frac{\phi_{ijk}^* - \phi_{ijk}^n}{\Delta t} = \Delta_h \phi_{ijk}^n, \tag{8}$$

where $\Delta_h \phi_{ijk}^n = (\phi_{i+1,jk}^n + \phi_{i-1,jk}^n + \phi_{i,j+1,k}^n + \phi_{i,j-1,k}^n + \phi_{ij,k+1}^n + \phi_{ij,k-1}^n - 6\phi_{ijk}^n)/h^2$. Next, we solve for reaction term (4) analytically using the method of separation of variables as follows:

$$\phi_{ijk}^{n+1} = \frac{\phi_{ijk}^*}{\sqrt{e^{-\frac{2\Delta t}{\epsilon^2}} + (\phi_{ijk}^*)^2(1 - e^{-\frac{2\Delta t}{\epsilon^2}})}}. \tag{9}$$
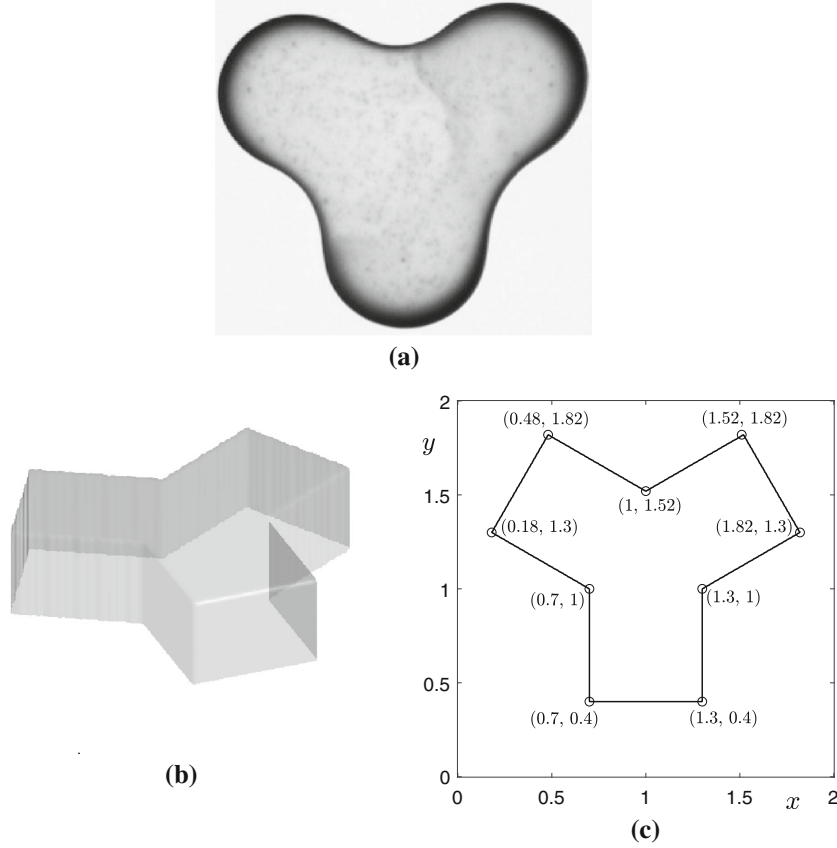
Fig. 13 a Nonaxisymmetric stain formation. Adapted from Deegan et al. [49] with permission from the Nature Publishing Group. **b** Initial shape of the irregular liquid droplet. **c** Cross-sectional view of the initial shape at $z = 0$, where the coordinates of each node are illustrated

A homogeneous Neumann boundary condition is imposed along the x- and y-directions as well as on the top boundary. The pinning boundary condition at the bottom boundary is defined as:

$$\phi_{ij0}^n = \phi_{ij1}^p \quad \text{for } 1 \leq i \leq N_x, \ 1 \leq j \leq N_y, \ n \geq p,$$

where p is the starting pinning time step. Figure 10 illustrates the pinning boundary condition at the bottom boundary [41].

4.3 Phase-field simulation for coffee-ring effect in regular 3D liquid droplets

We perform numerical simulations of the coffee-ring effect with coffee particles in regular 3D liquid droplets using the proposed method. The initial condition is set to $\phi(x, y, z, 0) = \tanh\left(\dfrac{1 - \sqrt{x^2 + y^2 + z^2}}{\sqrt{2}\epsilon}\right)$. The numerical parameters are used as $N_x = 80$, $N_y = 80$, $N_z = 40$, $h = 0.03$, $\Delta t = 0.125h^2$, $\epsilon = \epsilon_4$, $\gamma = 120$, $p = 0$, and $g = 20$. The number of coffee particles used in the numerical simulations was set to 5,000. The movement of the coffee particles follows a standard normal distribution in which the central 99% of the area under the curve lies within the mean ± 2.576 standard deviations. In Fig. 11, temporal evolutions are shown in which liquid evaporation and the movement of coffee particles occur simultaneously with a pinning boundary condition. The initial state and distribution of the coffee particles are shown in Fig. 11a. Figure 11b reveals the coffee-ring effect process. Figure 11c shows that ring-like coffee deposits gather at the boundary of the hemisphere. Additionally, we can also confirm the distribution of the coffee particles.

Next, we investigate the effect of the number of particles on the coffee-ring formation. The initial conditions and parameters take the same values as those described above. Coffee particle numbers of 1000, 5000, and
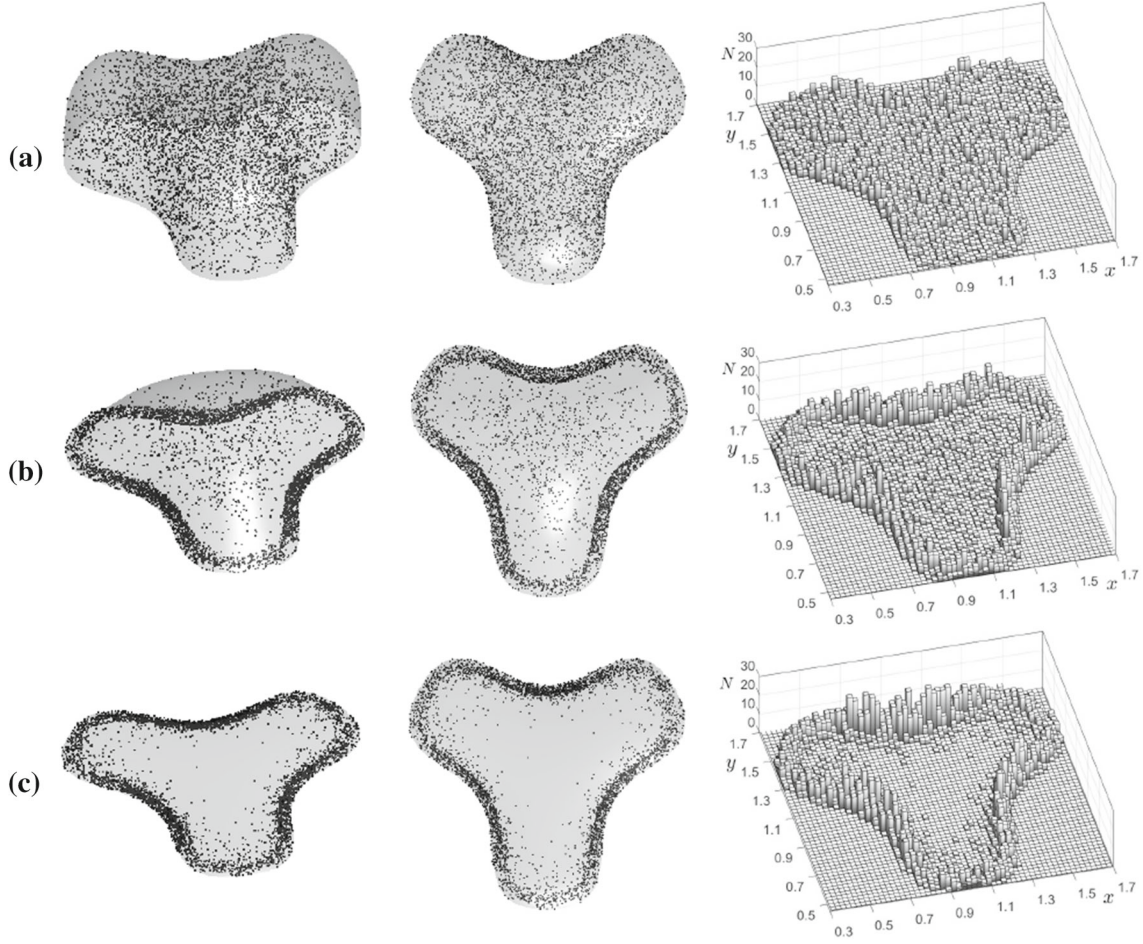
Fig. 14 Evolution of an irregular droplet and its particle distributions at **a** $t = 60\Delta t$, **b** $t = 300\Delta t$, and **c** $t = 1000\Delta t$

9000 are considered. Figure 12 illustrates temporal evolutions with respect to different particle numbers. The coffee ring becomes more obvious with an increasing number of coffee particles.

4.4 Coffee-ring formation within 3D irregular droplets

Furthermore, we consider the coffee-ring formation within irregular 3D liquid droplets in the domain $\Omega = (0, 2) \times (0, 2) \times (0, 1)$. Figure 13a illustrates the nonaxisymmetric stain formation [49]. The initial shape shown in Fig. 13b can be used to approximate the stain shape. We set an initial value of $\phi(x, y, z, 0) = 1$ inside the gray region in Fig. 13b. A corresponding cross-sectional view at $z = 0$ is shown in Fig. 13c, where the height ranges from $z = 0$ to $z = 0.55$. We set a value of $\phi(x, y, z, 0) = -1$ in all other regions. The numerical parameters used are $N_x = N_y = 54, N_z = 27, h = 0.037, \Delta t = 0.125h^2, \epsilon = \epsilon_4, \gamma = 120$, and $g = 20$. In the early stages of the simulation, the homogeneous Neumann boundary condition is used for the bottom boundary. The pinning effect begins at $t = 60\Delta t$, and we switch the homogeneous Neumann boundary condition to the pinning boundary condition. We set the initial distribution of coffee particles simultaneously. The number of coffee particles is 5500. Figure 14a, b, and c shows the evolutions of the droplet and corresponding particle distributions at $t = 60\Delta t, \ 300\Delta t$, and $1000\Delta t$, respectively. The coffee particles are observed to aggregate near the edge of the drying droplet.
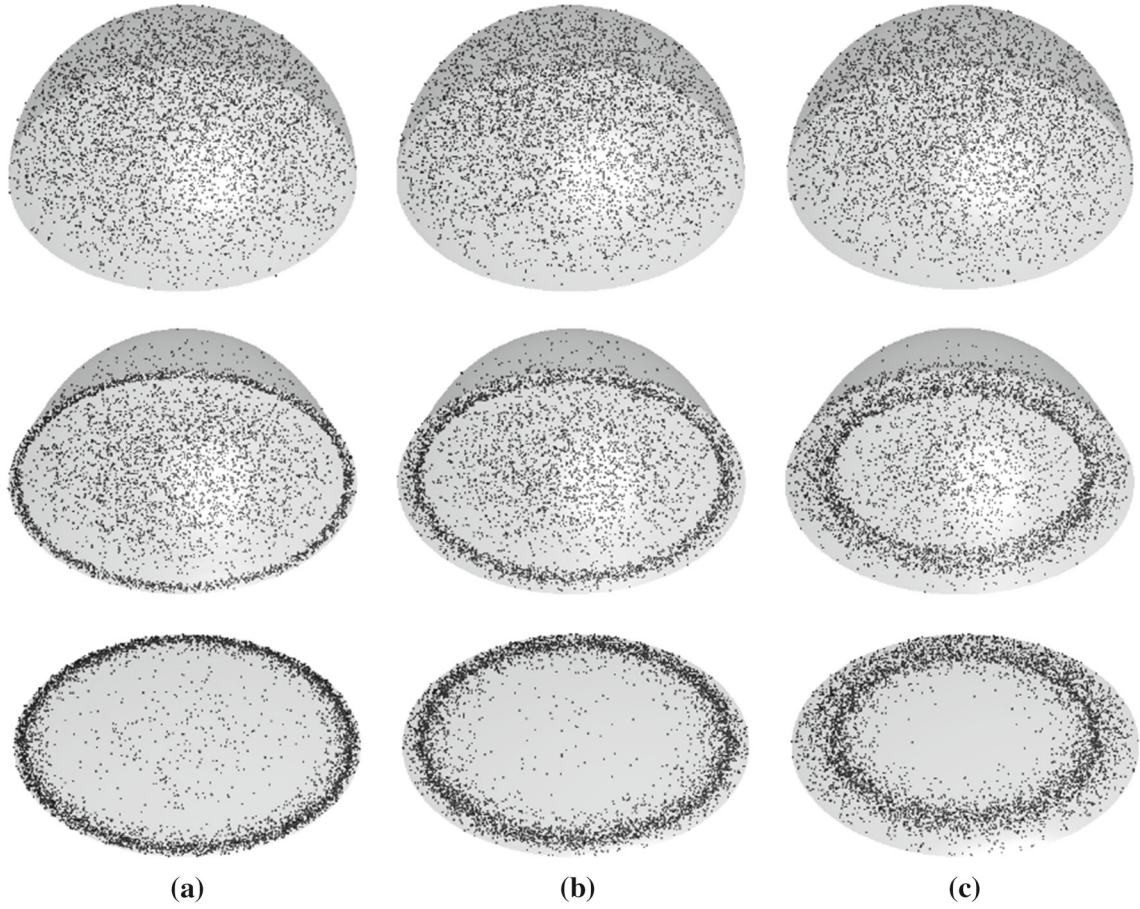
Fig. 15 Temporal evolutions of a droplet and particles with different values of ϵ: **a** ϵ_4, **b** ϵ_8, and **c** ϵ_{16}. The snapshots from the top to the bottom in each column are the results at $t = 0$, $500\Delta t$, and $3000\Delta t$, respectively

4.5 Effect of ϵ on the formation of coffee-ring

In the phase-field model, ϵ is an important parameter related to the thickness of the diffusive interface. A greater value of ϵ leads to a wider interfacial region, and a smaller value leads to a narrower interfacial region. As defined in Sect. 3, the size of the pinned region of particles is proportional to the value of ϵ. To analyze the effects of ϵ on the formation of coffee rings, we consider a droplet in 3D space with the same numerical parameters as those used in Sect. 4.3. Then, we compare the results with different values of ϵ: ϵ_4, ϵ_8, and ϵ_{16}. Figure 15a, b, and c shows the temporal evolutions with ϵ_4, ϵ_8, and ϵ_{16}, respectively. The pinned region is observed to become wider as the value of ϵ increases.

5 Conclusions

In this study, we proposed a novel computational model for the simulation of the coffee-ring phenomenon. We adopted a phase-field model and Monte Carlo simulation. The mean curvature flow of the AC equation with a pinning boundary condition was used to model drying droplets. The coffee particles inside the droplets moved according to random walk with a truncated standard normal distribution under gravitational force. We performed 2D and 3D computational experiments to demonstrate the ability of the proposed model to simulate the coffee-ring phenomenon. The results in the 2D space showed that greater values of α and g cause a larger number of particles to be accumulated in the pinned regions. Uniformly distributed particles in the initial stages were approximately equally accumulated in the two pinned regions. The results in the 3D space indicated that the coffee-ring region becomes wider with an increasing number of initial particles or value of ϵ. In future

works, we intend to investigate the formation of coffee-ring stains in large liquid drops under the effects of fluid flow and surface tension.

References

1. Sobac, B., Brutin, D.: Thermal effects of the substrate on water droplet evaporation. Phys. Rev. E **86**, 021602 (2012)
2. Leenaars, A.F.M., Huethorst, J.A.M., Van Oekel, J.J.: Marangoni drying: a new extremely clean drying process. Langmuir **6**, 1701 (1990)
3. Brutin, D., Sobac, B., Loquet, B., Sampol, B.: Pattern formation in drying drops of blood. J. Fluid Mech. **667**, 85–95 (2011)
4. Sobac, B., Brutin, B.: Structural and evaporative evolutions in desiccating sessile drops of blood. Phys. Rev. E **84**, 011603 (2011)
5. Kim, D., Jeong, S., Moon, J.: Organic thin film transistors with ink-jet printed metal nanoparticle electrodes of a reduced channel length by laser ablation. Appl. Phys. Lett. **91**, 071114 (2006)
6. Jing, J., Reed, J., Huang, J., Hu, X., Clarke, V., Edington, J., Housman, D., Anantharaman, T.S., Huff, E.J., Mishra, B., Porter, B., Shenker, A., Wolfson, E., Hiort, C., Kantor, R., Aston, C., Schwartz, D.C.: Automated high resolution optical mapping using arrayed, fluid-fixed DNA molecules. Proc. Natl. Acad. Sci. **95**, 8046 (1998)
7. Lal, S., Clare, S.E., Halas, N.J.: Nanoshell-enabled photothermal cancer therapy: impending clinical impact. Acc. Chem. Res. **41**, 1842–1851 (2008)
8. Skirtach, A.G., Dejugnat, C., Braun, D., Susha, A.S., Rogach, A.L., Parak, W.J., Mohwald, H., Sukhorukov, G.B.: The role of metal nanoparticles in remote release of encapsulated materials. Nano. Lett. **5**, 1371–1377 (2005)
9. Mugele, F., Baret, J.C.: Electrowetting: from basics to applications. J. Phys.: Condens. Matter **17**, R705–R774 (2005)
10. Murade, C.U., Oh, J.M., van den Ende, D., Mugele, F.: Electrowetting driven optical switch and tunable aperture. Opt. Express **19**, 15525–15531 (2011)
11. Chang, S.Y.P., Chao, Y.C.: Microemulsion polymerization of microlatex in sublimation ink for cotton fabric ink jet printing. J. Appl. Polym. Sci. **122**, 1872–1881 (2011)
12. Xue, C.H., Shi, M.M., Chen, H.Z., Wu, G., Wang, M.: Preparation and application of nanoscale microemulsion as binder for fabric inkjet printing. Colloid. Surf. A **287**, 147–152 (2006)
13. Kim, J.Y., Cho, K., Ryu, S.A., Kim, S.Y., Weon, B.M.: Crack formation and prevention in colloidal drops. Sci. Rep. **5**, 13166 (2015)
14. Tornero, A.F., Blasco, M.G., Azqueta, M.C., Acevedo, C.F., Castro, C.S., López, S.R.: Antimicrobial ecological waterborne paint based on novel hybrid nanoparticles of zinc oxide partially coated with silver. Prog. Org. Coat. **121**, 130–141 (2018)
15. Wu, Y., Lavernia, E.J.: Interaction mechanisms between ceramic particles and atomized metallic droplets. Metallurg. Trans. A **23**, 2923–2937 (1992)
16. Qu, R., Zhang, W., Liu, N., Zhang, Q., Liu, Y., Li, X., Wei, Y., Feng, L.: Antioil Ag_3PO_4 nanoparticle/polydopamine/Al_2O_3 sandwich structure for complex wastewater treatment: dynamics catalysis under natural light. ACS Sustain. Chem. Eng. **6**, 8019–8028 (2018)
17. Deegan, R.D., Bakajin, O., Dupont, T.F., Huber, G., Nagel, S.R., Witten, T.A.: Capillary flow as the cause of ring stains from dried liquid drops. Nature **389**, 827–829 (1997)
18. Conway, J., Korns, H., Fisch, M.R.: Evaporation kinetics of polystyrene bead suspensions. Langmuir **13**, 426–431 (1997)
19. Weon, B.M., Je, J.H.: Self-pinning by colloids confined at a contact line. Phys. Rev. Lett. **110**, 028303 (2013)
20. Bhardwaj, R., Feng, X., Attinger, D.: Pattern formation during the evaporation of a colloidal nanoliter drop: a numerical and experimental study. New J. Phys. **11**, 075020 (2009)
21. Boneberg, J., Burmeister, F., Schäfle, C., Leiderer, P., Reim, D., Fery, A., Herminghaus, S.: The formation of nano-dot and nano-ring structures in colloidal monolayer lithography. Langmuir **13**, 7080–7084 (1997)
22. Ondarçuhu, T., Joachim, C.: Drawing a single nanofibre over hundreds of microns. Europhys. Lett. **42**, 215–220 (1998)
23. Denkov, N.D., Velev, O.D., Kralchevsky, P.A., Ivanov, I.B., Yoshimura, H., Nagayama, K.: Mechanism of formation of two-dimensional crystals from latex particles on substrates. Langmuir **8**, 3183–3190 (1992)
24. Dimitrov, A.S., Dushkin, C.D., Yoshimura, H., Nagayama, K.: Observations of latex particle two-dimensional-crystal nucleation in wetting films on mercury, glass, and mica. Langmuir **10**, 432–440 (1994)
25. Vakaralski, I.U., Marston, J.O., Thoroddsen, S.T.: Foam-film-stabilized liquid bridge networks in evaporative lithography and wet granular matter. Langmuir **29**, 4966–4973 (2013)
26. Deegan, R.D.: Pattern formation on drying drops. Phys. Rev. E **61**, 475–485 (2000)
27. Deegan, R.D., Bakajin, O., Dupont, T.F., Huber, G., Nagel, S.R., Witten, T.A.: Contact line deposits in an evaporating drop. Phys. Rev. E **62**, 756–765 (2000)
28. Hu, H., Larson, R.G.: Marangoni effect reverses coffee-ring depositions. J. Phys. Chem. B **110**, 7090–7094 (2006)
29. Kim, H.S., Park, S.S., Hagelberg, F.: Computational approach to drying a nanoparticle-suspended liquid droplet. J. Nanopart. Res. **13**, 59–68 (2011)
30. Stannard, A.: Dewetting-mediated pattern formation in nanoparticle assemblies. J. Phys. Condens. Matter **23**, 083001 (2011)
31. Robbins, M.J., Archer, A.J., Thiele, U.: Modelling the evaporation of thin films of colloidal suspensions using dynamical density functional theory. J. Phys. Condens. Matter **23**, 415102 (2011)

32. Gupta, D., Peters, M.H.: A Brownian dynamics simulation of aerosol deposition onto spherical collectors. J. Colloid. Interface Sci. **104**, 375–389 (1985)
33. Chen, J.C., Kim, A.S.: Brownian dynamics, molecular dynamics, and Monte Carlo modeling of colloidal systems. Adv. Colloid. Interface Sci. **112**, 159–173 (2004)
34. Yunker, P.J., Still, T., Lohr, M.A., Yodh, A.G.: Suppression of the coffee-ring effect by shape-dependent capillary interactions. Nature **476**, 308–311 (2011)
35. Zhou, B., Heider, Y., Ma, S., Markert, B.: Phase-field-based modeling of the gelation process of biopolymer droplets in 3D bioprinting. Comput. Mech. **63**, 1187–1202 (2019)
36. Shao, Y., Duan, Q., Qiu, S.: Adaptive consistent element-free Galerkin method for phase-field model of brittle fracture. Comput. Mech. **64**, 741–767 (2019)
37. Yin, B., Kaliske, M.: Fracture simulation of viscoelastic polymers by the phase-field method. Comput. Mech. **65**, 293–309 (2020)
38. Chiu, P.H.: A coupled phase field framework for solving incompressible two-phase flows. J. Comput. Phys. **392**, 115–140 (2019)
39. Soligo, G., Roccon, A., Soldati, A.: Mass-conservation-improved phase field models for turbulent multiphase flow simulation. Acta Mech. **230**, 683–696 (2019)
40. Zhu, G., Kou, J., Sun, S., Yao, J., Li, F.: Numerical approximation of a phase-field surfactant model with fluid flow. J. Sci. Comput. **80**, 223–247 (2019)
41. Lee, H.G., Yang, J., Kim, J.: Pinning boundary conditions for phase-field models. Commun. Nonlinear Sci. Numer. Simul. **82**, 105060 (2020)
42. Kim, J.: Phase-field models for multi-component fluid flows. Commun. Comput. Phys. **12**, 613–661 (2012)
43. Long, J., Luo, C., Yu, Q., Li, Y.: An unconditional stable compact fourth-order finite difference scheme for three dimensional Allen-Cahn equation. Comput. Math. Appl. **77**, 1042–1054 (2019)
44. Saka, H., Bengston, R.D., Reichl, L.E.: Relaxation of Brownian particles in a gravitational field. Am. J. Phys. **77**, 240–243 (2009)
45. Barr, D.R., Sherrill, E.T.: Mean and variance of truncated normal distributions. Am. Stat. **53**, 357–361 (1999)
46. Codling, E.A., Bearon, R.N., Thorn, G.J.: Diffusion about the mean drift location in a biased random walk. Ecology **91**, 3106–3113 (2010)
47. Mazzeo, D., Oliveti, G., Labonia, E.: Estimation of wind speed probability density function using a mixture of two truncated normal distributions. Renew. Energy **115**, 1260–1280 (2018)
48. Shur, V.Y., Bykov, D.A., Mingaliev, E.A., Tyurnina, A.E., Burban, G.V., Kadushnikov, R.M., Mizgulin, V.V.: Coffee ring effect during drying of colloid drop: experiment and computer simulation. Ferroelectrics **476**, 47–53 (2015)
49. Deegan, R.D., Bakajin, O., Dupont, T.F., Huber, G., Nagel, S.R., Witten, T.A.: Capillary flows as the cause of ring stains from dried liquid drops. Nature **389**, 827–829 (1997)